Chinese Chemical Letters 36 (2025) 110350

Contents lists available at ScienceDirect

Chinese Chemical Letters

journal homepage: www.elsevier.com/locate/cclet

A self-propelled nanovesicle with robust antibacterial and regeneration-promoting capabilities for treating biofilm-induced periodontitis

Bairui Zeng[a,1], Zhixiang Mu[a,1], Tianxi Shen[a], Xiaoliang Qi[b,c], Yuanqi Chen[a], Kezheng Lei[a], Chen Huang[a], Yi Wang[a], Rongdang Hu[a], Xiaojun Cai[a,*], Jianliang Shen[b,c,*], Hui Deng[a,*]

[a] School and Hospital of Stomatology, Wenzhou Medical University, Wenzhou 325027, China
[b] National Engineering Research Center of Ophthalmology and Optometry, Eye Hospital, Wenzhou Medical University, Wenzhou 325027, China
[c] Zhejiang Engineering Research Center for Tissue Repair Materials, Wenzhou Institute, University of Chinese Academy of Sciences, Wenzhou 325001, China

ARTICLE INFO

Article history:
Received 17 June 2024
Revised 18 August 2024
Accepted 19 August 2024
Available online 22 August 2024

Keywords:
Polymer vesicles
Biofilm
Nitric oxide
Gas therapy
Periodontitis

ABSTRACT

In the fight against bacterial infections, it is critical to effectively disrupt biofilms. However, disruption of biofilms becomes exceptionally difficult due to the low permeability of therapeutic agents. Herein, we present a self-propelled nanovesicle (PCL-PLG@CHX) strategy for eliminating biofilms and further expediting the healing of wounds. PCL-PLG@CHX is synthesized by assembling vesicles from amphiphilic polymers, which incorporate both poly-ε-caprolactone and guanidinated-poly-ε-lysine (PCL-PLG) and are infused with chlorhexidine (CHX). Upon application to sites of bacterial infection, PCL-PLG@CHX, abundant in guanidinium structures, effectively accumulates on the negatively charged surface of biofilms. It interacts with reactive oxygen species (ROS) within the biofilm, leading to nitric oxide (NO) production. The generated NO cannot only propel the nanovesicle to penetrate deeper into the biofilm, but also act as a signaling molecule to disperse the biofilm, working in conjunction with the subsequent release of CHX for an enhanced antibacterial impact. Following the eradication of bacteria, the residual guanidine component continues to produce small quantities of NO, facilitating angiogenesis and epithelial growth, thereby accelerating the healing of wounds. Together, our study shows that PCL-PLG@CHX utilizes the potential of guanidine moieties to efficiently break down biofilms and support tissue restoration, tackling the pivotal challenge of biofilm-related diseases.

The rising incidence of periodontitis, identified as the sixth most prevalent chronic inflammatory ailment [1,2], coupled with its significant link to chronic noncommunicable illnesses like diabetes and cerebrovascular disorders [3,4], has sparked heightened focus. Dental plaque, a sophisticated microbial biofilm resulting from bacterial buildup on tooth and root surfaces, is identified as the primary trigger for periodontitis [2,5]. This biofilm initiates inflammation in the surrounding periodontal tissues, causing destruction, bone loss, and eventual tooth loss [5,6]. Traditionally, the cornerstone of periodontitis management has been the mechanical eradication of the biofilm. However, achieving total removal of the plaque biofilm from hard-to-reach areas, like periodontal pockets and root bifurcations, poses a significant challenge. Furthermore, the propensity of bacteria to re-establish themselves often calls for the use of supplementary antibacterial therapies. Systemic antibiotics, such as tetracycline and metronidazole, have been employed [7]. Regrettably, oral pathogens tend to form complex and thick plaque biofilms, which not only protect the bacteria against the host's immune defenses but also block antibacterial agents from penetrating, thus enhancing bacterial resistance [5,6]. Clinically, biofilm-associated infections often require 100- or 1000-fold higher dosages of antibiotics, resulting in numerous adverse side effects such as decreased immune response and microflora imbalance [8–10]. Therefore, penetrating the biofilm barrier is crucial for enhancing the effectiveness of antibacterial infection treatments.

Lately, micro- and nanomotors have garnered considerable interest because of their self-propelled movement and have been explored for performing diverse functions, such as drug delivery, biosensing and therapeutic diagnoses [11,12]. Nanomotors, through

* Corresponding authors.
E-mail addresses: cxj520118@aliyun.com, cxj520118@wmu.edu.cn (X. Cai), shenjl@wiucas.ac.cn (J. Shen), dh0726@163.com (H. Deng).
[1] These authors contributed equally to this work.

https://doi.org/10.1016/j.cclet.2024.110350
1001-8417/

their improved penetration effect and targeted delivery of antibacterial substances, can effectively dismantle biofilms. Maric and colleagues have demonstrated a photothermal-driven nanomotor adorned with gold nanoparticles that successfully breaches the biofilm matrix and disrupts its structure [13]. Wang *et al.* developed chitosan-based micromotors using water-soluble magnesium metals with significant inhibition and removal of bacterial biofilms [14]. Pumera and colleagues developed a photodynamic ZnO micromotor featuring chemically customizable properties aimed at biofilm eradication [15]. Despite this innovative work, nanomotors encounter various obstacles: (1) Employment of harmful metal ions like Mn^{2+} and Cu^{2+} could negatively impact healthy tissues; (2) Nanomotors activated by near-infrared light frequently experience inadequate tissue depth penetration; (3) Continuous external stimuli are required for the propulsion of nanomotors. Consequently, innovating a new targeted antibiofilm nanomotor to overcome these hurdles is critically important.

Recent research indicates that commensal bacteria play a role in controlling opportunistic pathogens *via* bioactive products such as H_2O_2 (500 μmol/L) [16–18]. Furthermore, the inherent production of H_2O_2 in biofilms could be better shielded from salivary lactoperoxidases, which might fail to infiltrate preformed biofilms, resulting in a concentration gradient between the plaque's surface and its depth [19,20]. Consequently, developing a chemotaxis system that capitalizes on the reactive oxygen species (ROS) concentration gradient within biofilms holds the potential for effective biofilm permeation. Notably, it has been demonstrated in recent studies that guanidino groups can interact with ROS to generate nitric oxide (NO) owing to their exceptional affinity for ROS [21]. Exploiting this unique property, nanovesicle incorporating guanidino groups can achieve positive chemotaxis towards the concentration gradients of ROS, thereby facilitating effective penetration into biofilms.

In addition, NO interacts with ROS to produce reactive nitrogen oxides possessing significant antimicrobial properties, demonstrating substantial promise for the healing of infected wounds [22,23]. Compared to other antimicrobial compounds, NO can use different pathways (*e.g.*, protein dysfunction, DNA breaks and lipid peroxidation) to directly eliminate bacteria without fostering drug resistance [24,25]. More importantly, NO can act as a biofilm dispersal molecule, leading to c-di-GMP degradation, which increases bacterial motility and reduces adhesion and extracellular polymeric substance production, thus comprehensively destroying biofilms [26]. Besides its antibacterial properties, NO can also enhance swift wound recovery by boosting collagen synthesis and encouraging angiogenesis throughout skin reconstruction [27,28].

To address the challenge of effectively penetrating biofilms within deep periodontal pockets, we developed an innovative nanovesicle system powered by NO named PCL-PLG@CHX (Scheme 1). This system employs a multifaceted approach, simultaneously facilitating biofilm penetration, offering NO-based sterilization, and enhancing pro-angiogenic effects through a unified mechanism. Essentially, the foundational vesicles, referred to as PCL-PLL, were crafted through amphiphilic polymer self-assembly, specifically poly-ε-caprolactone and poly-ε-lysine (PCL_{40}-PLL_{30}). Subsequently, the reaction of these vesicles with 1*H*-pyrazole-1-carboxamidine hydrochloride catalysed by *N*,*N*-diisopropylethylamine produced guanidinium-based polymer vesicles, PCL-PLG. These newly formed vesicles can encapsulate chlorhexidine (CHX), a premier choice for oral antibacterial treatment. The PCL-PLG@CHX system is expected to demonstrate exceptional capabilities in biofilm penetration and destruction. Specifically, PCL-PLG@CHX is designed to produce NO swiftly in reaction to elevated levels of ROS present within the biofilm, which not only propels the nanovesicle but also aids in biofilm dispersion. Furthermore, the synergistic antibacterial action of NO and CHX, released from the vesicles, aims at reducing the required dosage of antibacterial medications. Lastly, the controlled

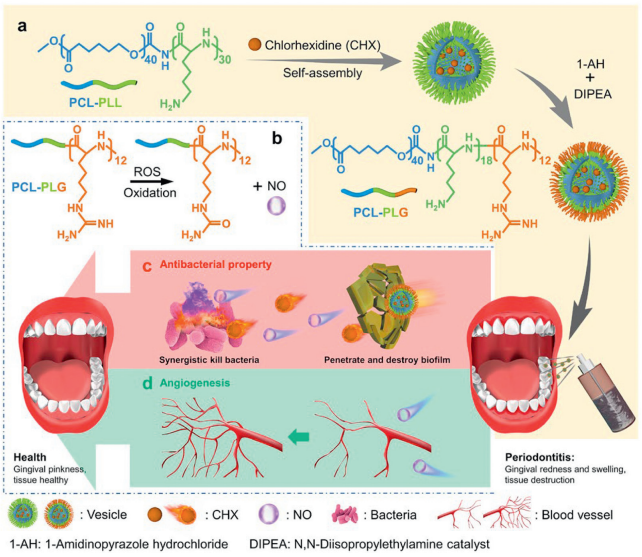

Scheme 1. Vesicle formation steps and the dual roles in antimicrobial action and tissue healing enhancement.

release of NO from the remnants of PCL-PLG@CHX in body tissues is anticipated to stimulate collagen synthesis and aid in the regeneration of blood vessels [29].

PCL_{40}-PLL_{30} underwent self-assembly *via* nanoprecipitation, resulting in the creation of PCL-PLL vesicles. These vesicles were then subjected to guanidination using DIPEA and 1-amidinopyrazole hydrochloride, leading to the formation of PCL-PLG vesicles adorned with guanidine moieties. The efficiency of the granitization process was estimated at around 40%, determined by contrasting the integration of the proton peak adjacent to the guanidine moiety (2.84 ppm) against the PCL peak (3.52 ppm), as illustrated in Fig. S1 (Supporting information). Through this process, twelve primary amines in PCL-PLL underwent a transformation into guanidine groups. Vesicles encapsulating CHX within PCL-PLL and PCL-PLG were termed PCL-PLL@CHX and PCL-PLG@CHX, respectively. Transmission electron microscopy (TEM) showcased their uniform spherical shape, revealing their hollow structures with an average diameter close to 200 nm (Fig. 1a), which is conducive to encapsulating drugs. Dynamic light scattering (DLS) analysis corroborated the TEM findings, with PCL-PLL and PCL-PLG vesicle sizes measured at roughly 221 and 224 nm. Post-loading with CHX, the vesicles' diameters expanded to about 245 nm (Figs. 1b and c), likely due to the electrostatic repulsion between the positively charged CHX and the vesicles' amino groups. In addition, the success of the guanidino process is indirectly demonstrated by the fact that the guanidino group is positively charged and the zeta potential of the PCL-PLL rises from 22.3 mV to 40.2 mV after guanidinoisation (Fig. 1d).

Physiological metabolic activities of bacteria in biofilms can generate ROS, such as H_2O_2, with concentrations up to 500 μmol/L [16–18]. Additionally, immune cells also release ROS to combat bacteria and toxins, further increasing the concentration of ROS within biofilms [30]. H_2O_2 present in biofilms can oxidize guanidine functionalities, leading to NO production. The generation of NO by these vesicles was quantified in solution *via* a Griess reagent kit, modified for accuracy. With higher concentrations of H_2O_2, NO output from the vesicles showed a corresponding increase. Specifically, exposure to 100 μmol/L H_2O_2 catalyzed the creation of nearly 20 μmol/L NO within 1 h (Fig. 1e). Moreover, the presence of CHX in PCL-PLG@CHX vesicles did not alter their NO-producing capacity, mirroring the performance of PCL-PLG alone (Fig. 1e). When subjected to a simulated biofilm environment rich in H_2O_2 (100

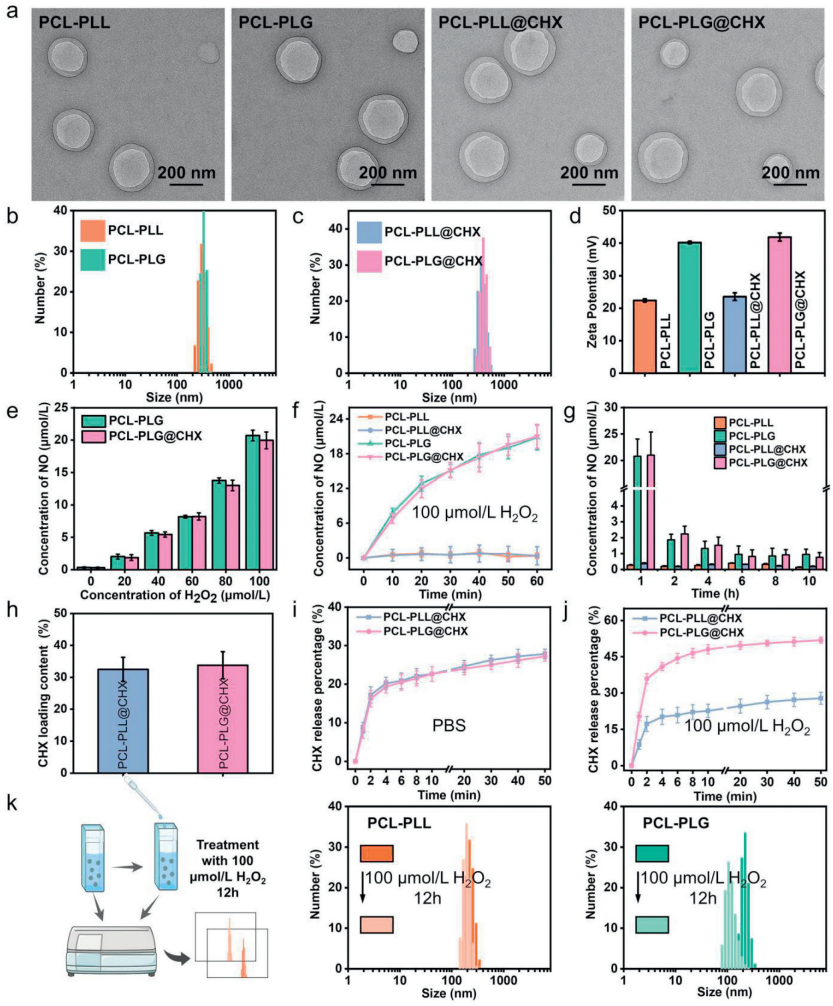

Fig. 1. Characterization of the vesicles. (a) TEM visuals of vesicles post uranyl acetate staining (2.0%). (b, c) Analysis of vesicle size distribution *via* DLS. (d) Measurement of vesicle zeta potential. (e) Comparative NO production by various vesicles under different H_2O_2 concentrations. Analysis of NO production from vesicles in the presence of 100 μmol/L H_2O_2 over short (f) and extended (g) periods. (h) Quantification of CHX encapsulated within PCL-PLL@CHX and PCL-PLG@CHX vesicles. Release dynamics of CHX from vesicles in PBS, with (j) and without (i) 100 μmol/L H_2O_2. (k) Vesicle size variations pre and post 12-h interaction with 100 μmol/L H_2O_2. Results are shown as mean ± standard deviation (SD) ($n = 3$).

μmol/L), both vesicle variants reached a bactericidal NO concentration of 6 μmol/L in just 10 min (Fig. 1f) [31]. Notably, PCL-PLG vesicles demonstrated a dual function: triggering NO release under high H_2O_2 conditions and neutralizing ROS, thus protecting cells and tissues from oxidative stress [32,33]. The antimicrobial properties of NO are dose-dependent. At low concentrations (typically less than 1 μmol/L), NO has limited bactericidal effects, but it has demonstrated a strong ability to promote tissue regeneration [24,25,34]. Over time, NO levels tapered off as H_2O_2 and guanidine were consumed, maintaining a lower NO concentration beneficial for tissue healing and vascular growth (Fig. 1g). The CHX encapsulation efficiency in PCL-PLL@CHX and PCL-PLG@CHX was determined through ultraviolet–visible–near infrared (UV–vis–NIR) spectrophotometer and CHX calibration curves, with results showing 32.5% ± 3.78% and 33.8% ± 4.23% loading (Fig. 1h and Fig. S2 in Supporting information). CHX release kinetics were assessed in both normal (phosphate buffered saline, PBS) and oxidative (100 μmol/L H_2O_2) conditions, revealing a faster release from PCL-PLG@CHX in oxidative environments — 45% in the initial 10 min, compared to a more stable release in standard conditions (Figs. 1i and j). The differential release rates suggest that the vesicles' stability in various environments influences CHX discharge [34,35]. After 12 h in a H_2O_2-enriched PBS solution, PCL-PLL vesicles maintained their size, whereas PCL-PLG shrank from 224 nm to 113 nm (Fig. 1k), illustrating the impact of guanidine oxidation on vesicle integrity and consequent accelerated CHX release [35]. Such H_2O_2-responsive behavior underscores the vesicles' potential for precise therapeutic delivery in biofilm-infected and healthy tissues alike, promoting bacterial clearance and tissue recovery [36].

Considering the safety of PCL-PLG@CHX for clinical application, a thorough analysis of the vesicles in terms of biosafety was conducted both *in vitro* and *in vivo*. Evaluations of biocompatibility were conducted through cell counting kit-8 (CCK-8) and hemolysis tests. Findings from CCK-8 evaluations indicated that vesicle doses under 40 μg/mL did not produce cytotoxic effects on cellular structures (Figs. S3a and S4 in Supporting information). In parallel, hemolysis tests revealed that similar concentrations of vesicles avoided causing damage to cell membranes (Fig. S3b and Fig. S5 in Supporting information). Given the design of PCL-PLG@CHX for dental applications, the potential for patients to inadvertently ingest the formulation was considered. In an experimental setup, rats received oral administration of 10 mL PCL-PLG@CHX solution at a concentration of 40 μg/mL or a comparable volume of PBS across three days. Observations on rat body weight and the health status of vital organs were made over a ten-day pe-

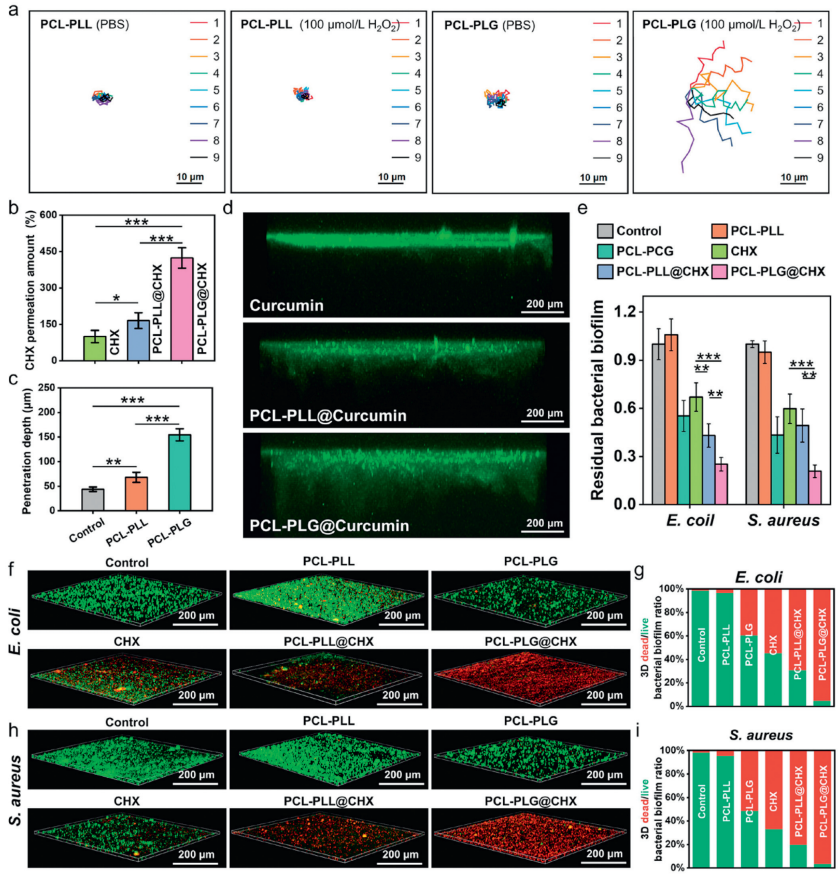

Fig. 2. Anti-biofilm effect of vesicles. (a) Normalized movement trajectories of PCL-PLL nanovesicle and PCL-PLG nanovesicle in PBS with or without H_2O_2. (b) CHX diffusion throughout the biofilm. (c) Data analysis on penetration depths. (d) Exploration of curcumin and its vesicle formulations' biofilm infiltration, highlighted by curcumin's green luminescence. (e) Biofilm integrity assessment *via* spectrophotometric absorbance readings at 595 nm. (f) *E. coli* biofilm disintegration. (g) Examination of *E. coli* presence in biofilm structures. (h) Disruption effects on *S. aureus* biofilms. (i) Analysis of *S. aureus* occupancy in biofilm matrices. Results are shown as mean ± SD ($n = 3$). $^{*}P < 0.05$, $^{**}P < 0.01$, $^{***}P < 0.001$.

riod. No observable differences in weight or behavior were noted when compared to control group rats (Fig. S6 in Supporting information). Histopathological examination using hematoxylin-eosin (H&E) staining showed no significant tissue alterations or inflammation in critical organs, including the spleen, kidneys, heart, lungs, and liver, post-administration (Fig. S3c in Supporting information). Consequently, the PCL-PLG@CHX vesicles exhibit high levels of biocompatibility and safety, affirming their potential for use in medical treatments.

Bacteria predominantly form biofilms within the body, leading to various illnesses, including enteritis and periodontitis. For antibacterial agents to effectively combat these infections, penetrating biofilms is essential [9,37]. Nanomotors offer a solution by facilitating improved penetration into biofilms. In our research, confocal laser scanning microscopy (CLSM) was employed to monitor the dynamics of fluorescein isothiocyanate (FITC)-labelled nanovesicles in PBS solution, both in the presence and absence of 100 μmol/L H_2O_2. PCL-PLL showed minimal movement in the PBS solution, while the PCL-PLG nanovesicle exhibited enhanced diffusion in the presence of H_2O_2 (Fig. 2a). This indicates that PCL-PLG can effectively generate NO by reacting with ROS, enabling the autonomous motion of PCL-PLG nanovesicle in physiological environments. The autonomous motion of these nanovesicles facilitates the delivery of antibacterial drugs into biofilms.

To assess CHX diffusion into biofilms, separate additions of CHX, PCL-PLL@CHX, and PCL-PLG@CHX were made. After a 2-h incubation period, biofilms underwent washing, collection, and disruption to measure the total CHX absorption. The investigation revealed a minimum fourfold increase in CHX absorption with PCL-PLG@CHX compared to the solo CHX application (Fig. 2b), showcasing the superior biofilm penetration capabilities of PCL-PLG. This enhancement was further examined using CLSM for visualizing drug penetration depth within the biofilms. Given CHX's lack of fluorescence, curcumin was utilized both alone and within vesicles as a comparative measure for vesicular biofilm penetration. Findings indicated that curcumin predominantly accumulated at the biofilm's exterior in the control scenario, highlighting the biofilm's effectiveness in hindering the ingress of external agents like antibiotics, thereby diminishing the antibacterial efficacy of such drugs [38]. Within the biofilm, the PCL-PLL variant demonstrated a diminished fluorescence, indicating that its amino groups moderately enhanced biofilm penetration. Contrarily, the PCL-PLG variant displayed a permeation increase of at least fourfold, evidenced by a pronounced fluorescence beneath the biofilm layer (Figs. 2c and d). This notable improvement in biofilm penetration by PCL-PLG is credited to its guanidine-rich exterior, surpassing the permeation abilities provided by amino groups [25]. Furthermore, the guanidino component reacts with ROS present in the biofilm to generate NO, which provides the propulsive force necessary for vesicle movement. This action facilitates deeper movement into the biofilm, improving the dispersion and penetration through the biofilm's defensive layers [23,39]. Consequently, interactions between the vesicles and bacterial cells were significantly enhanced, leading to more effective bacterial eradication. Additionally, the biofilm's density was reduced, favorably affecting CHX's penetration capability.

We assessed the biofilm breakdown through crystalline violet staining techniques. The PCL-PLG@CHX cohort demonstrated a significantly reduced biofilm presence relative to other comparative groups (Fig. 2e and Fig. S9 in Supporting information). Moreover, employing PCL-PLL@CHX for treatment achieved superior biofilm reduction when juxtaposed with CHX alone, challenging previous observations concerning antiplanktonic bacterial effects. This observation underscores the critical role of biofilm penetration. Subsequently, the bacterial vitality within the biofilm was evaluated using Live/Dead staining methods. The presence of dead bacteria was highlighted in red *via* propidium iodide (PI) staining, whereas viable bacteria appeared green as a result of SYTO9 staining. In typical biofilm structures, a pronounced green fluorescence denoted a substantial quantity of viable bacteria. Biofilms treated with CHX exhibited only surface-level red fluorescence, indicating CHX's restricted penetration capabilities. Conversely, the group treated with PCL-PLL@CHX showed dead bacteria throughout and on the biofilm's exterior. Furthermore, within the PCL-PLG@CHX treated biofilms, an overwhelming majority of the bacteria were eliminated, as illustrated in Figs. 2f–i. These results collectively underscore the exceptional ability of PCL-PLG@CHX to eradicate biofilms, attributable to several key factors: (1) The presence of numerous guanidine groups on the surface enhances PCL-PLG@CHX's penetration into biofilms [23]; (2) The elevated ROS levels within the biofilm catalyze the swift production of copious NO by PCL-PLG@CHX's guanidine groups. This generation of NO aids in further dispersion by promoting deeper infiltration into the biofilm [25]; (3) The concerted release of both CHX and NO within the biofilm not only precipitates the swift demise of bacteria but also facilitates the biofilm's effective breakdown [41]. Consequently, the synergy of guanidine moieties, CHX and NO in this advanced nanovesicle amplifies its anti-biofilm and bactericidal properties. Such a novel strategy offers significant promise for treating conditions like periodontitis, where biofilms are a principal contributing factor.

Initially, the minimum inhibitory concentration (MIC) test was employed to evaluate the antibacterial effectiveness of the vesicles against growing planktonic bacteria. Test organisms included *Staphylococcus aureus* (*S. aureus*) and *Escherichia coli* (*E. coli*). Vesicles were co-incubated with bacteria overnight using the broth microdilution approach. MIC values were ascertained by recording the optical density at 600 nm (OD_{600}), with findings depicted in Fig. S7 (Supporting information). CHX, renowned for its extensive antibacterial and bactericidal properties against numerous bacterial species, stands as the treatment of choice for oral antibacterial purposes in clinical settings. This investigation revealed that a mere 4 μg/mL concentration of CHX significantly inhibited bacterial proliferation, aligning with outcomes observed in clinical settings, as shown in Figs. S7a and b [40]. However, the antibacterial performance of PCL-PLL@CHX at an equivalent CHX concentration exhibited a marginally reduced effect, likely due to the incomplete discharge of CHX. For PCL-PLG@CHX to match the antibacterial impact, a concentration of 8 μg/mL was necessary, where the actual CHX quantity dispensed was only 1.97 μg/mL, substantially below the MIC for CHX. This adjustment lowers the CHX amount needed, aiming to decrease adverse effects like taste alteration and mucous membrane discoloration [41]. Based on the MIC data (Fig. S7) alongside biocompatibility evaluations (Figs. S4 and S5 in Supporting information), a vesicle concentration of 20 μg/mL, encapsulating roughly 6 μg/mL of CHX, was selected for future experiments, with 6 μg/mL of CHX acting as the benchmark control.

Given that OD600 readings fail to differentiate living from deceased bacteria, a bacterial colony enumeration test was conducted to evaluate vesicles' antibacterial efficacy. Figs. 3a–c depict that PCL-PLL showed minimal antibacterial action, eliminating merely 10% of free-floating bacteria. CHX, at a dosage of 6 μg/mL, succeeded in exterminating over 90% of such bacteria. Conversely, PCL-PLG demonstrated moderate antibacterial strength, managing to eradicate 70% of the planktonic bacterial population. Notably, treatment with PCL-PLG@CHX resulted in the complete elimination of bacteria, suggesting that PCL-PLG@CHX possesses superior antibacterial activity. Moreover, the combination of NO and CHX synergistically eradicated bacteria with high efficiency. Live/Dead staining was utilized to more precisely determine bacterial mortality following vesicle intervention. Figs. 3d–f reveal a significant presence of red fluorescence in *E. coli* and *S. aureus* after CHX application, signifying substantial disruption to their cellular membranes. In contrast, exposure to PCL-PLG@CHX resulted in almost all *E. coli* and *S. aureus* cells displaying bright red fluorescence due to PI staining, indicating severe damage to their membranes. Further examination of bacterial structural changes was performed using scanning electron microscopy (SEM). PCL-PLL treatments had minimal impact on the bacterial form, leaving *E. coli* and *S. aureus* cells with smooth, unaltered membranes. Conversely, CHX application noticeably compromised bacterial membrane integrity, causing the outer surface to become rough and slightly shrunken. Bacteria subjected to PCL-PLL@CHX showed some level of membrane damage, albeit less than those treated with CHX alone. Most notably, PCL-PLG@CHX inflicted extreme harm to the bacterial membranes, with many cells losing their shape entirely and rupturing, resulting in significant protein loss, as illustrated in Fig. 3g.

Findings from both the colony counting assay and SEM evaluations concurred, underscoring PCL-PLG@CHX's exceptional antibacterial performance. Such effectiveness is linked to the electrostatic pull from PCL-PLG@CHX's guanidine units, which carry a substantial positive charge and engage with bacterial cells. Additionally, these guanidine structures produce NO when ROS are present, amplifying the antimicrobial impact in conjunction with the CHX discharged from the vesicles [25,30]. Additionally, the bactericidal effect of the vesicles on the periodontal pathogen *P. gingivalis* was assessed using bacterial live-dead staining and SEM. The results demonstrated that PCL-PLG@CHX exhibited excellent bactericidal efficacy against *P. gingivalis* (Figs. S8a–c in Supporting information).

The development of new blood vessels is crucial for tissue repair, as they facilitate the delivery of oxygen and nutrients to the injured area [42,43]. NO is recognized as an essential molecule for promoting vascular regeneration and the expansion of tube-like structures [42,44]. In our research, we analyzed the angiogenic potential of PCL-PLG@CHX utilizing human umbilical vein endothelial cells (HUVECs). To replicate physiological scenarios in which vesicles quickly release NO due to elevated ROS levels within the biofilm, followed by a gradual release of NO at lower concentrations by remaining vesicles under normal ROS levels, we pretreated the vesicles in PBS containing 100 μmol/L H_2O_2 for one hour. The treated samples were then utilized to create a 20% conditioned medium for HUVEC incubation (Fig. S10a in Supporting information). We evaluated the biocompatibility of these vesicles through Live/Dead staining and the CCK-8 assay. The biocompatibility of these vesicles was found to be on par with initial observations (Figs. S10b–d in Supporting information). Our prior investigations into the vesicles' long-term NO release capabilities *in vitro* revealed their consistent production of minor NO quantities over an extended period (Figs. 1f and g). Next, we employed fluorescent probes to detect intracellular NO levels. The findings, illustrated in Fig. S11a (Supporting information), showed that NO fluorescence intensity was notably higher in both PCL-PLG and PCL-PLG@CHX sets compared to controls, suggesting that vesicles could enter cells and produce additional NO when encountering intracellular ROS. The angiogenic capacity of vesicles was assessed through a tube formation experiment. Following a 4-h incubation on matrigel, capillary-like structures were observed across all six HUVEC groups. Analysis of the tube formation assay indicated a notably

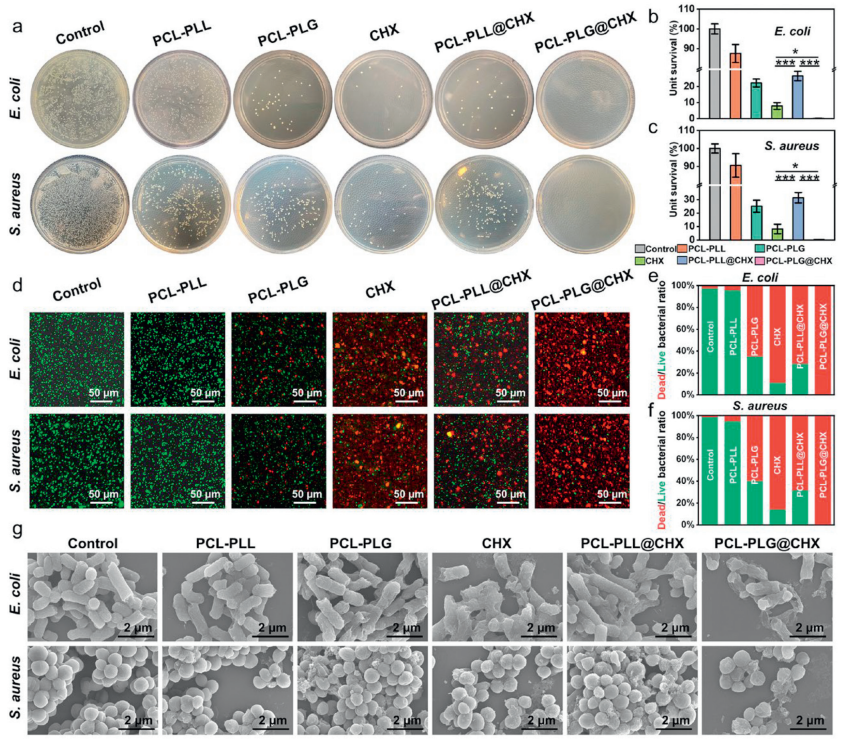

Fig. 3. The vesicles' bactericidal efficacy. (a) Illustrative images of different groups with antimicrobial coatings. *E. coli* (b) and *S. aureus* (c) survival percentages for each group. (d) Fluorescent microscopy visualizations depicting viable bacteria in green (SYTO9) and nonviable in red (PI) across treatments. Ratios of live to dead bacteria for *E. coli* (e) and *S. aureus* (f). (g) SEM visuals showcasing the interaction between *E. coli* or *S. aureus* and the different treatment modalities. Results are shown as mean ± SD ($n = 3$). $^{*}P < 0.05$, $^{***}P < 0.001$.

higher count of tubes and tube junctions in the vascular networks by HUVECs treated with PCL-PLG and PCL-PLG@CHX compared to those in alternate groups, as depicted in Figs. S11b and S12 (Supporting information). Furthermore, the similarity in outcomes between the PCL-PLG and PCL-PLG@CHX groups implies that CHX's inclusion did not hinder vascular regeneration, highlighting that angiogenic capability largely stems from NO generated by PCL-PLG. Subsequent exploration into vascularization mechanisms *via* qRT-PCR and western blot assessments showed an elevation in markers of angiogenesis (vascular endothelial growth factor, VEGF) and maturation (CD31) in both PCL-PLG and PCL-PLG@CHX sets in comparison to those devoid of NO (Fig. S13 in Supporting information). These findings affirm NO's pivotal role in modulating pro-angiogenic cytokines. Importantly, VEGF, a critical mediator of angiogenesis, is implicated in NO synthesis regulation, enhancing NO levels through endothelial nitric oxide synthase induction [45]. Such a reciprocal enhancement loop significantly boosts NO's angiogenic effects, promoting the expansion and maturation of vascular endothelial cells identified by CD31, thereby encouraging new blood vessel formation.

Motivated by its *in vitro* antibacterial and vascular regeneration capabilities, the efficacy of PCL-PLG@CHX in promoting healing and combating bacteria was further assessed in rat models afflicted with skin wound infections. Animal studies received approval following the regulations and guidelines of the Institutional Animal Care and Use Committee at Wenzhou Medical University, with the approval number WYDW2021-0196. Circular lesions (10 mm) were inflicted on the rats' dorsal, followed by inoculation with the *S. aureus* solution to simulate models of wound infection. Subsequent to model creation, lesions were cleansed with the specified solution across three days (Fig. S14a in Supporting information). The healing trajectory for each group was meticulously monitored on days 1, 3, 6, and 9, as depicted in Fig. S14b (Supporting information). Notably, the PCL-PLG@CHX-treated rats showcased superior healing speeds devoid of any pronounced inflammatory reactions to the infection. Conversely, in the PBS-treated control group, a significant number of wounds remained open, exhibiting bleeding, inflammation, and pus formation during the initial three days post-operation, with scab formation not occurring until day 6. Wounds treated with CHX and PCL-PLL@CHX displayed inflammatory discharges yet did not significantly bleed or develop sepsis. The wounds addressed with PCL-PLG@CHX, however, commenced drying and scabbing by the third day (Fig. S14b). Figs. S14c and d (Supporting information) illustrate the contraction of the wounds. Throughout the evaluation period, PCL-PLG@CHX's ability to enhance healing was markedly superior. In terms of antibacterial performance, exudates from the wounds were collected on the second day for bacterial colony enumeration, thereby assessing the antibacterial effectiveness *in vivo*. The control set saw a high colony count, whereas the CHX application notably reduced bacterial presence. PCL-PLG@CHX, aligning with *in vitro* antibacterial outcomes, displayed the most potent antibacterial activity (Fig. S15 in Supporting information).

To evaluate the healing process of wounds in rats, tissues harvested on the ninth day underwent histological examination. H&E staining highlighted that the PCL-PLG@CHX-treated set experienced the most advanced re-epithelialization and dermal repair, evidenced by the seamless development of epidermal layers atop the tissue (Figs. S17 and S19a in Supporting information). Detailed tissue analysis showed superior epithelial structure maturity and enhanced skin appendage formation in the PCL-PLG@CHX-treated specimens compared to others. Additionally, this group showed significant angiogenic activity, with mature blood vessels housing red blood cells, facilitating nutrient and oxygen delivery essential for tissue repair (Fig. S17II). Analysis through Masson's trichrome staining indicated minimal collagen presence, characterized by loosely organized fibers in the PBS and PCL-PLL sets, while

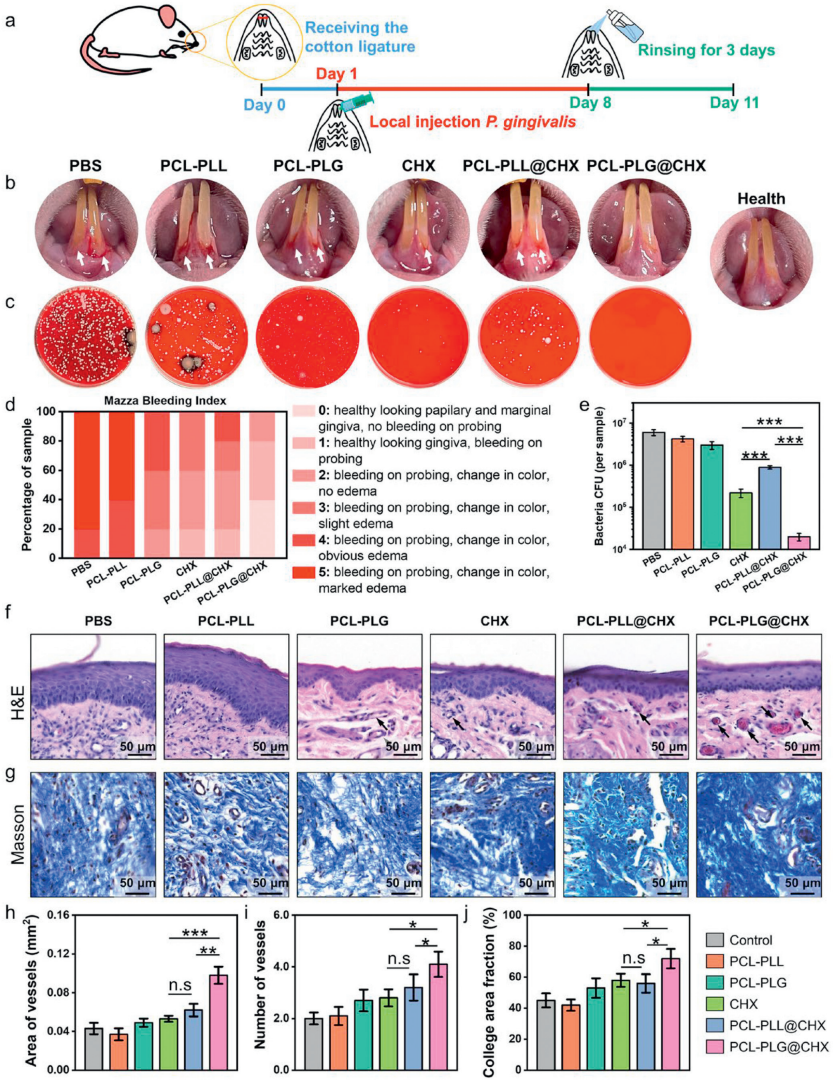

Fig. 4. Effects of vesicle therapy on rat periodontitis. (a) Overview of periodontitis model development and therapeutic approach: around the anterior lower teeth's cervical margins, a 4-0 cotton thread was tied. Next, 10 μL of LPS was injected below the gum line near the lower incisors continuously for a week. The cotton threads were then removed, followed by a three-day application of either vesicle-based or CHX solutions to cleanse the periodontal areas. (b) Images from inside the mouth. (c) Aerobic culture photographs of *P. gingivalis* harvested from rat periodontal regions on blood agar after three days. (d) Evaluation using the Mazza bleeding index for clinical diagnosis. (e) Proportion of surviving bacteria counts per specimen. (f) Histological examination with H&E staining of periodontal regions, with black arrows highlighting the formation of new blood vessels. (g) Staining of periodontal areas using Masson's trichrome technique. (h, i) Quantitative evaluation of vessel count (h) and vascular area (i) in H&E stained samples. (j) Evaluation of collagen concentration in samples colored with Masson's trichrome stain. Results are shown as mean ± SD ($n = 3$). $^{*}P < 0.05$, $^{**}P < 0.01$, $^{***}P < 0.001$. n.s, not significant.

the CHX and PCL-PLL@CHX groups presented with denser collagen. The PCL-PLG@CHX group stood out with its tightly packed, well-organized collagen fibers, showcasing the highest density (Figs. S19a and S20a in Supporting information). Further evaluation using CD31 immunofluorescence staining, a benchmark for angiogenesis, confirmed the highest neovascularization in the PCL-PLG@CHX group (Figs. S19b and S20b in Supporting information). These outcomes strongly suggest that PCL-PLG@CHX excels in suppressing biofilm formation and enhancing skin repair in models of infectious skin defects.

We have successfully demonstrated the potential of PCL-PLG@CHX as an antibacterial nanovesicle that exhibits increased anti-biofilm activity promotes tissue regeneration, and effectively treats infected skin wounds. Addressing periodontitis involves tackling complexities beyond those encountered with open skin wounds. Periodontitis frequently results in the development of deep periodontal pockets harboring dense bacterial biofilms [46,47]. The existence of bone and root bifurcations within these pockets further complicates the environment, posing challenges to pharmacological interventions [46,47]. To examine the effectiveness of PCL-PLG@CHX against periodontitis, an *in vivo* model was established by encircling the cervical margin of the lower front teeth with a ligature and introducing *P. gingivalis* through local injection. Within a week, rat models of periodontitis were ready, receiving various nanomedicine treatments over three days. The *in vivo* experimentation process is depicted in Fig. 4a. Post-treatment, the rats were sedated for clinical evaluation of periodontal health using a probe, focusing on the Mazza bleeding index, which ranges from 0 to 5 based on severity [48,49]. Observations indicated that the gingiva in the control group showed signs typical of periodontitis, such as redness and bleeding (Fig. 4b). Both control and PCL-PLL sets scored between 3 and 5 on the Mazza scale, reflecting severe symptoms (Fig. 4d). The CHX group, considered the clinical benchmark, displayed slight redness and minimal bleeding. Remarkably, the PCL-PLG@CHX group showed negligible gingival redness or swelling, mirroring the healthy group's condition

(Figs. 4b and d). Analysis of gingival crevicular fluid highlighted PCL-PLG@CHX's superior antibacterial performance, aligning with findings from skin wound infection studies (Figs. 4c and e). The outcomes of treatments using CHX and PCL-PLL@CHX displayed minor variations compared to results obtained from *in vitro* studies, likely due to the oral cavity's complex environment and the challenge of maintaining effective treatment presence.

NO, a crucial endogenous signaling molecule, plays essential roles in immune modulation and the enhancement of wound repair processes [25,44]. Its involvement includes the orchestration of inflammatory cell mobilization and the modulation of pro-inflammatory mediators during the healing phases [24]. To evaluate the histological characteristics of gingival tissues and the prevalence of inflammatory cells, H&E staining was utilized. The analysis, as depicted in Fig. 4f, revealed pronounced infiltration by inflammatory cells in the control group experiencing inflammation, whereas sites of inflammation in alternative groups showed a reduction in such cells. Particularly, the group treated with PCL-PLG@CHX was noted for having the minimal presence of inflammatory cells across all tested groups. This decrease is attributed to the efficient removal of biofilms, thereby reducing the triggers for inflammation. The findings further underscore the significant anti-inflammatory capabilities of NO *in vivo*, facilitating a shift from inflammatory conditions to those conducive to regeneration (Fig. 4f) [50]. Additionally, NO's role in stimulating the regeneration of blood vessels contributes to improved nutrient delivery to the damaged sites, thereby hastening the healing process [44]. The examination of H&E stained sections indicated a surge in angiogenesis and an increase in vessel formation within the PCL-PLG@CHX treated group compared to others (Fig. 4f). A semi-quantitative assessment of the tissue histology affirmed a notable enhancement in both vascular area and the count of vessels in the PCL-PLG@CHX treated specimens relative to counterparts (Figs. 4h and i).

Pathogenic bacteria in the biofilm lead to an increase in collagenase, resulting in significant degradation of collagen fibers in periodontal tissues [5,6]. Type I collagen, predominant in the periodontal membranes, is known to have its expression enhanced by external NO sources [51]. Within a NO-emitting environment, stem cells are capable of producing substances that aid in tissue regeneration and have immunomodulatory effects [52]. Consequently, Masson's trichrome staining was employed to evaluate both the degradation and recovery of collagen at the inflammation site (Figs. 4g and j). In both groups administered with CHX and those treated with PCL-PLL@CHX, there was noticeable preservation of collagen fibers, likely due to the successful bacterial clearance. Noteworthy was the exceptional preservation of collagen within the PCL-PLG@CHX group, showcasing dense, well-organized fibers (Fig. 4g). This superior outcome is credited to the comprehensive bacterial removal and NO release, which encourages the renewal of type I collagen and the formation of new blood vessels, thus expediting the healing process. These observations lead to the conclusion that PCL-PLG@CHX significantly enhances wound recovery through two mechanisms: effective bacterial elimination *via* biofilm disruption and the combined antibacterial effect, alongside the sustained release of trace amounts of NO that fosters angiogenesis and collagen restoration.

We developed a self-propelled nanovesicle (PCL-PLG@CHX) designed to navigate the complexities of removing biofilms in deep periodontal pockets while offering a stepwise solution for antibacterial action and tissue regeneration. The PCL-PLG@CHX system consists of vesicles abundant in guanidinium (PCL-PLG), characterized not only by their outstanding ability to penetrate biofilms owing to guanidine groups but also as a potent NO generator. Upon encountering high ROS concentrations present in the biofilm, these vesicles containing CHX within PCL-PLG undergo a reaction where the guanidine groups are oxidized, resulting in the production of NO. This process aids in the release of CHX directly into the biofilm, thereby reducing the required CHX dosage and mitigating potential side effects while effectively fighting bacteria and clearing the biofilm. Crucially, after eradicating bacteria from periodontal spaces, the remaining guanidine compounds generate trace NO upon interaction with standard ROS concentrations, facilitating angiogenesis and epithelial regeneration of the wound area, thus markedly enhancing the recovery process. To conclude, our constructed NO self-propelled PCL-PLG@CHX nanovesicle leverages the unique properties of guanidine to achieve triple effects: biofilm penetration, sterilization, and promotion of angiogenesis. Most importantly, the guanidinium-based nanovesicle strategy, powered by a ROS gradient, offers a simple yet efficient solution and a fresh perspective on treating various inflammatory diseases through chemotaxis targeting.

Declaration of competing interest

The authors declare that they have no known competing financial interests or personal relationships that could have appeared to influence the work reported in this paper.

CRediT authorship contribution statement

Bairui Zeng: Writing – original draft, Project administration, Investigation, Data curation. **Zhixiang Mu:** Writing – original draft, Project administration, Investigation, Funding acquisition, Data curation. **Tianxi Shen:** Visualization, Validation, Methodology, Investigation. **Xiaoliang Qi:** Writing – review & editing, Formal analysis. **Yuanqi Chen:** Software. **Kezheng Lei:** Investigation. **Chen Huang:** Validation. **Yi Wang:** Formal analysis. **Rongdang Hu:** Supervision, Project administration. **Xiaojun Cai:** Supervision, Methodology, Conceptualization. **Jianliang Shen:** Writing – review & editing, Resources. **Hui Deng:** Writing – review & editing, Resources, Funding acquisition, Conceptualization.

Acknowledgments

This work was supported by the Wenzhou Major Scientific and Technological Innovation Project (No. ZY2022020), the Zhejiang Provincial Science and Technology Project for Public Welfare (No. LGF22H140010), and the Science and Technology Plan of Wenzhou (No. H20210008).

Supplementary materials

Supplementary material associated with this article can be found, in the online version, at doi:10.1016/j.cclet.2024.110350.

References

[1] P.I. Eke, W.S. Borgnakke, R.J. Genco, Periodontology 2000 82 (2019) 257–267.
[2] Y. Cui, G. Tian, R. Li, et al., J. Periodontol. 94 (2023) 193–203.
[3] R.J. Genco, M. Sanz, Periodontology 2000 83 (2020) 7–13.
[4] R.J. Genco, W.S. Borgnakke, Periodontology 2000 83 (2020) 40–45.
[5] N.S. Jakubovics, S.D. Goodman, L. Mashburn-Warren, G.P. Stafford, F. Cieplik, Periodontology 2000 86 (2021) 32–56.
[6] X. Li, C. Yu, B. Zhang, et al., NPJ Biofilms. Microbio. 9 (2023) 75.
[7] D. Herrera, A.J. van Winkelhoff, P. Matesanz, K. Lauwens, W. Teughels, Periodontology 2000 (2023), doi:10.1111/prd.12492.
[8] S. Chen, Z. Zhang, L. Wei, et al., Chin. Chem. Lett. 34 (2023) 108412.
[9] X. He, L. Dai, L. Ye, et al., Adv. Sci. 9 (2022) 2105223.
[10] Z. Li, D. Xu, Z. Deng, et al., Chem. Eng. J. 452 (2023) 139587.
[11] C. Ghosh, S. Ghosh, A. Chatterjee, et al., Nat. Commun. 14 (2023) 5903.
[12] H. Tian, J. Lin, F. Zhu, et al., Chin. Chem. Lett. 34 (2023) 107577.
[13] T. Maric, A. Løvind, Z. Zhang, J Geng, A Biosen, Adv. Healthc. Mater. 12 (2023) 2203018.
[14] J.A.M. Delezuk, D.E. Ramírez-Herrera, B. Esteban-Fernández de Ávila, J. Wang, Nanoscale 9 (2017) 2195–2200.
[15] M. Ussia, M. Urso, K. Dolezelikova, et al., Adv. Funct. Mater. 31 (2021) 2101178.

[16] Y. Huang, Y. Liu, S. Shah, et al., Biomaterials 268 (2021) 120581.
[17] L. Zhu, J. Kreth, Oxid. Med. Cell. Longevity 2012 (2012) 717843.
[18] X. Liu, M.M. Ramsey, X. Chen, et al., Proc. Natl. Acad. Sci. U. S. A. 108 (2011) 2668–2673.
[19] T. Thurnheer, R. Gmur, S. Shapiro, B. Guggenheim, Appl. Environ. Microbiol. 69 (2003) 1702–1709.
[20] A. Magán-Fernández, S.M. Rasheed Al-Bakri, F. O'Valle, et al., Cells 9 (2020) 1494.
[21] T. Li, Z. Liu, J. Hu, et al., Adv. Mater. 34 (2022) 2206654.
[22] H. Cai, X. Wu, L. Jiang, et al., Chin. Chem. Lett. 35 (2024) 108946.
[23] Y. Yang, J. Wang, S. Huang, et al., Natl. Sci. Rev. 11 (2024) nwae044.
[24] J. Zhu, J. Tian, C. Yang, et al., Small 17 (2021) 2101495.
[25] M. Qi, X. Ren, W. Li, et al., Nano Today 43 (2022) 101447.
[26] K.P. Rumbaugh, K. Sauer, Nat. Rev. Microbiol. 18 (2020) 571–586.
[27] Z. Zhou, Y. Liu, W. Li, et al., Adv. Healthc. Mater. 13 (2023) 2302153.
[28] S. Yao, Y. Wang, J. Chi, et al., Adv. Sci. 9 (2021) 2103449.
[29] F. Hassanzadeh-Afruzi, M. Azizi, I. Zare, et al., Chin. Chem. Lett. 35 (2024) 109564.
[30] Z. Yuan, C. Lin, Y. He, et al., ACS Nano 14 (2020) 3546–3562.
[31] H. He, T. He, Z. Zhang, et al., Chin. Chem. Lett. 29 (2018) 1497–1499.
[32] Y. Yang, M. Li, G. Pan, J Chen, B Guo, Adv. Funct. Mater. 33 (2023) 2214089.
[33] S. Wang, K. Yu, Z. Yu, et al., Chin. Chem. Lett. 34 (2023) 108184.
[34] Y. Dai, Y. Ding, L. Li, et al., Chin. Chem. Lett. 32 (2021) 2715–2718.
[35] L. Chen, H. Zhao, S. Xue, K. Chen, Y. Zhang, Foods 11 (2022) 1630.
[36] X. He, J.T. He, X. Sun, et al., Adv. Funct. Mater. 32 (2022) 2203964.
[37] D. Hu, Y. Deng, F. Jia, Q Jin, J Ji, ACS Nano 14 (2019) 347–359.
[38] B. Trubenová, D. Roizman, A. Moter, et al., Trends Microbiol 30 (2022) 841–852.
[39] Z. Wang, A. Jin, Z. Yang, et al., ACS Nano 17 (2023) 8935–8965.
[40] H.L. Htun, P.Y. Hon, M.T.G. Holden, B. Ang, A. Chow, Clin. Microbiol. Infec. 25 (2019) 1154.
[41] F. Poppolo Deus, A. Ouanounou, Int. Dent. J. 72 (2022) 269–277.
[42] J.C. Doverspike, S.J. Mack, A. Luo, et al., ACS Appl. Mater. Interfaces 12 (2020) 44475–44484.
[43] N. Tang, R. Zhang, Y. Zheng, et al., Adv. Mater. 34 (2021) 2106842.
[44] L. Huang, J. Zhang, X. Liu, et al., Chin. Chem. Lett. 32 (2021) 234–238.
[45] Y. Liu, M. Paterson, S.L. Baumgardt, et al., Cardiovasc. Res. 115 (2019) 168–178.
[46] J. Luan, R. Li, W. Xu, et al., Acta Pharm. Sin. B 13 (2023) 2310–2333.
[47] D.D. Bosshardt, Periodontol. 2000 76 (2018) 43–50.
[48] J.E. Mazza, M.G. Newman, T.N. Sims, J. Clin. Periodontol. 8 (1981) 203–212.
[49] Q. He, Z. Mu, A. Shrestha, et al., Oral Dis. 28 (2021) 1936–1946.
[50] M.Q. Man, J.S. Wakefield, T.M. Mauro, P.M. Elias, Inflammation 45 (2022) 949–964.
[51] J. Chen, D. Sheng, T. Ying, et al., Nano Micro Lett. 13 (2020) 23.
[52] D. Mitra, E.T. Kang, K.G. Neoh, ACS Appl. Mater. Interfaces 12 (2019) 21159–21182.